EES Batteries

PAPER

View Article Online
View Journal

Cite this: DOI: 10.1039/d6eb00077k

Insight and regulation of interfacial coordination chemistry of a high-voltage $LiCoPO_4$ cathode *via* functionalized carbon layer anchoring for robust surface passivation

Moohyun Woo and George P. Demopoulos *

Lithium cobalt phosphate ($LiCoPO_4$, LCP) is a high-voltage (high-V) polyanionic compound, of critical importance for its high energy density. However, LCP's application has been hampered by inferior coulombic efficiency and capacity retention owing to cathode degradation triggered by the elevated cut-off voltage of 5.0 V *vs.* Li/Li^+. Namely, such high-V leads to severe parasitic side reactions at the cathode–electrolyte interface involving complex phenomena, the understanding of which holds the key to designing robust high-V cathodes. Herein, post-mortem analysis of cycled LCP electrodes under different aging conditions revealed the fundamental capacity fading mechanism at high-V interfaces. Detrimental degradation occurs through redox metal (RM) dissolution, caused by undesired electrochemical and chemical reactions with the electrolyte. This process induces cation vacancies, leading to lattice collapse and progressive structural ingress. To combat this, we successfully engineered a sucrose-derived functionalized carbon layer (FCL) anchoring strategy to regulate interfacial coordination chemistry. This conductive FCL layer serves a dual role: (i) expediting charge-transfer kinetics by establishing an efficient electronic network and (ii) anchoring surface cations, thereby promoting a protective inorganic-enriched cathode–electrolyte interphase (CEI) layer characterized by Li–F and Co–F species while suppressing organic ligand-induced dissolution. This passivation suppresses structural ingress and preserves the olivine structure, resulting in significantly enhanced rate capability and cycling stability.

Received 7th April 2026,
Accepted 30th May 2026

DOI: 10.1039/d6eb00077k

rsc.li/EESBatteries

Broader context

The proliferation of autonomous systems and robotics requires next-generation batteries capable of delivering extreme energy density and rapid-charging kinetics. Lithium cobalt phosphate ($LiCoPO_4$, LCP) is uniquely positioned to meet these rigorous demands for niche applications as it shares the robust olivine framework yet offers a significantly higher operating voltage to surpass current energy limits. However, its commercial viability remains restricted by accelerated interfacial decay and severe chemical instability at the electrode–electrolyte boundary under high-voltage (high-V) operation. To address these challenges, comprehensive post-mortem analyses were performed to elucidate interfacial degradation, leading to the application of interfacial coordination chemistry control *via* a functionalized carbon layer (FCL) coating. This versatile and scalable protocol stabilizes high-V cathodes through a synergistic defense mechanism that can be seamlessly integrated into various cathode production lines. By providing new insight and straightforward surface coating method, this work opens a rewarding pathway towards the development of high-V cathodes for demanding energy storage applications.

Introduction

The rise of energy-intensive applications, ranging from grid-scale energy storage systems (ESS) to unmanned aerial vehicles (UAVs) and robotics, has driven the demand for next generation Li-ion batteries (LIBs) beyond the current energy density level.[1–4] To surpass these energy thresholds, it is essential to develop advanced cathode materials based on several selection criteria including operating voltage, storage capacity, rate capability, and cycling stability.[5–7] Design and development of high-voltage (high-V) cathodes is identified as a critical step in the pursuit for high energy density LIBs.[8] In this context, lithium cobalt phosphate ($LiCoPO_4$, LCP) is of great interest as a high-V polyanionic compound with a high theoretical energy density of 800 Wh kg^{-1} thanks to the redox voltage and capacity (4.8 V × 167 mAh g^{-1}) properties.[9] Additionally, LCP, like its commercial counterpart lithium iron phosphate ($LiFePO_4$, LFP), belongs to the olivine crystal structure family, boasting a robust framework.[10,11] These attributes, despite its cobalt (Co) content, have made LCP a strong candidate for

Materials Engineering, McGill University, 3610 rue University, Montréal, QC H3A 0C5, Canada. E-mail: george.demopoulos@mcgill.ca

niche applications where high energy density systems are critical.[12,13]

Despite these promising benefits, the development of LCP cathodes has been hampered by certain compromising inherent material properties: (1) intrinsically low ionic and electronic conductivities causing sluggish kinetics, (2) abundant anti-site defects blocking the one-dimensional (1-D) Li-ion diffusion pathway, and (3) capacity fading predominantly due to interphasial degradation at high-V, a relatively less explored yet critical contributor requiring further investigations.[14–16] Recently, we have developed a novel crystal variety of LCP characterized by a shortened Li-ion diffusion length attributed to preferential crystal growth and a defect-free structure.[17] This architecture, realized *via* solvent molecule-crystal plane regulation and subsequent argon (Ar)-annealing, enables the achievement of a nearly theoretical full discharge capacity and remarkable rate capability. In spite of these significant bulk-level improvements, high-V interfacial instability stands as a critical bottleneck, where persistent capacity fading upon prolonged cycling indicates that electrolyte decomposition seemingly negates the protection offered by high-V stabilizing electrolyte additives. This observation implies that capacity fading is not merely an acceleration of electrolyte decomposition, but rather a result of intricate and multifaceted interfacial side reactions that remain poorly understood. Accordingly, fundamental and comprehensive post-mortem investigations are required in various electrochemical environments with different aging/cycling conditions at the raised cut-off voltage, to provide insights as to the origin of LCP capacity fading. At the same time, research into surface engineering to mitigate destructive electrode–electrolyte interfacial reactions *via* proper functional surface coating is of great urgency to improve charge transport kinetics and prevent capacity fading *via* interface stabilization.

In this work, we scrutinized the correlation between capacity fading and irreversible interfacial reactions by conducting extensive post-mortem analysis. Our investigation reveals that the interfacial degradation of LCP proceeds through considerable redox metal (RM) dissolution under relatively long-term cycling operations. These side reactions lead to progressive lattice collapse and structural ingress into the particle interior. This degradation is primarily driven by chelating organic compounds as a result of electrolyte oxidation at the elevated voltage. These compounds coordinate with and extract LCP surface cations from the olivine framework, leaving behind interfacial defects responsible for the observed capacity fading. To mitigate this, we developed a sucrose-derived functionalized carbon layer (FCL) anchoring strategy that provides multi-functional passivation through synergistic mechanisms. The FCL substantially stabilizes the interface through a tailored coordination chemistry, beyond its intrinsic role of a carbon layer in facilitating charge-transfer kinetics and serving as a physical barrier against direct electrolyte contact. Notably, oxygen-containing functional groups on FCL anchor surface cations *via* strong coordination, which actively promotes the formation of a robust inorganic-enriched cathode–electrolyte interphase (CEI) layer characterized by Li–F and Co–F species. This newly evolved interphase further reinforces the interfacial stability by effectively preventing the chelation by organic ligands. Consequently, our strategy demonstrates remarkable rate capability, achieving nearly theoretical Li-ion storage capacities across all C-rates, ranging from C/10 to 1C. Remarkably, at 1C rate, it delivers an outstanding discharge capacity of 163.0 mAh g^{-1} (equivalent to 771.2 Wh kg^{-1} in energy density) and relatively enhanced retention (76.36% after 100 cycles).

Results and discussion

Irreversible interfacial aging of $LiCoPO_4$ upon cycling

Structural and compositional variation at the electrode–electrolyte interface was probed *via* post-mortem HRTEM, HAADF, and elemental mapping techniques and the obtained results are compiled in Fig. 1a–f. Pristine LCP prior to high-V operation (Fig. 1a) displays a smooth surface topography without any observable features of foreign precipitates. However, HRTEM images (Fig. 1b and c) reveal the formation of a thicker CEI layer at the slower rate, C/10 compared to 1C. This rate-dependency indicates that the prolonged high-V exposure upon charge–discharge process promotes further electrolyte decomposition, leading to the remarkable CEI layer growth. Furthermore, HAADF and elemental mapping (Fig. 1d–f) demonstrate a stark contrast between pristine and cycled electrodes, as evidenced by gradual topographic roughening and foreign elemental deposition arising from these parasitic side reactions.[18–21] Pristine LCP (Fig. 1d) retains its intact surface topography, consistent with the HRTEM result (Fig. 1a), while exhibiting only a trace amount of fluorine (F) due to PVDF binder, alongside the constituent elements of LCP including cobalt (Co), phosphorus (P), and oxygen (O). On the other hand, cycled LCP (Fig. 1e and f) shows pronounced topographic roughening and markedly elevated F concentration, both indicative of irreversible interfacial degradation as a result of side reactions with the electrolyte. As this degradation progresses, parasitic ingress into LCP bulk crystals emerges, resulting in the graded zoning in the sub-surface region. This phenomenon could imply that RM dissolution (leaching) occurs concurrently with CEI layer evolution, as will be further elucidated in the following sections.

Thermogravimetric analysis (TGA) further substantiates topographic and compositional alterations, providing complementary validation of the mass evolution associated with the rate-dependent interfacial degradation. The weight loss for the pristine and cycled electrodes (Fig. 1g and Fig. S1) can be categorized into four distinct temperature regimes, each attributed to the thermal response of specific components: (i) absorbed water (H_2O) evaporation (25–100 °C), which is negligible because of the storage in an Ar-filled glovebox (<0.5 ppm of H_2O and O_2); (ii) CEI layer dissociation (100–250 °C); (iii) PVDF binder decomposition (250–500 °C); and (iv) acetylene black combustion (above 500 °C).[22,23] After the heat treatment, the

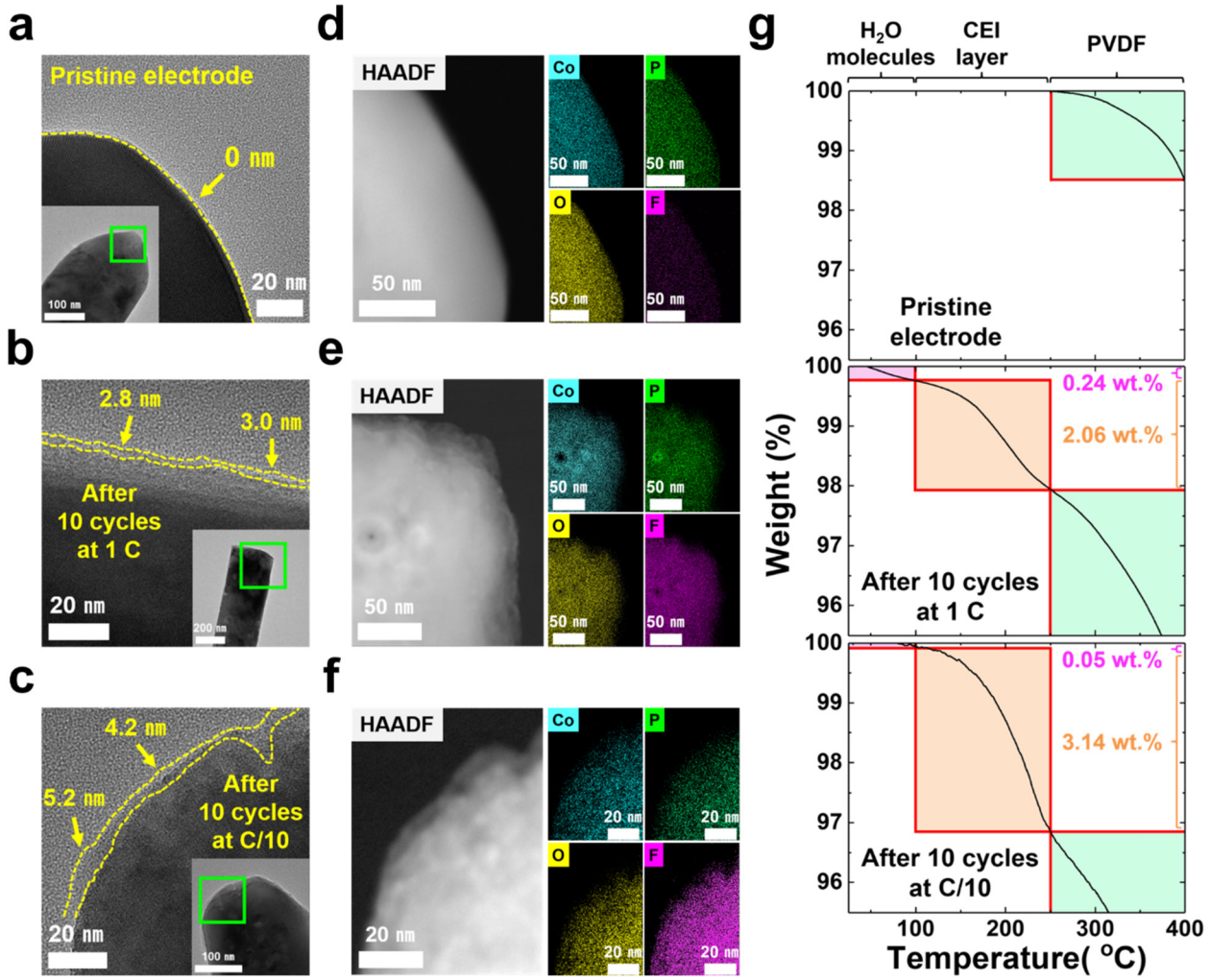

Fig. 1 (a–c) HRTEM images displaying CEI layer evolution from the pristine state to after 10 cycles at 1C and C/10; (d–f) the corresponding HAADF and elemental mapping (Co, P, O, and F) images; and (g) the respective TGA curves up to 400 °C.

final mass remained is almost 70 wt% accurately corresponding to the ratio of LCP active material in the electrode composition. For further investigation, the TGA profile below 400 °C was analyzed in detail to assess CEI layer evolution upon electrochemical cycling. Considering the pristine electrode as a baseline, we can clearly see the weight loss involved with PVDF to occur above 250 °C. Yet, there is another discernible weight loss occurring in the temperature range, 100–250 °C for both cycled electrodes at 1C (2.06 wt%) and C/10 (3.14 wt%) that must be assigned to the quantity of the newly evolved CEI layer. The overall TGA results (Fig. S1c) also provide indirect evidence of RM dissolution (signaled by parasitic ingress shown in Fig. 1f) given that the mass of the cycled LCP active material drops below 70 wt% after the heat treatment. Typically, the CEI layer consists of organic compounds and poorly crystalline materials with relatively low atomic weights. In contrast, dissolution of Co-containing species from the Co–P–O framework would theoretically result in more significant mass loss due to the higher atomic weight of Co. This theoretical consideration supports interpreting the sub-70 wt% final mass as an indirect indicator of Co dissolution, providing a reasonable scientific basis drawn from our obtained data. Accordingly, these findings underscore the urgent need for a surface functionalization strategy to passivate the LCP interface and suppress irreversible RM dissolution.

One-step facile surface coating with a functionalized carbon layer

To mitigate the irreversible side reactions at the interface, we introduced a surface coating strategy to protect the LCP surface. For this purpose, different amounts of sucrose (30, 40, and 50 wt%) were employed as a carbon source and dissolved in D.I. water, to which solvothermally-synthesized LCP (ST-LCP) powder was added and agitated. The coated LCP was obtained after drying and annealing in an Ar atmosphere, following the same protocol established for solvothermally-synthesized and Ar-annealed LCP (referred to as ST-A-LCP).[17]

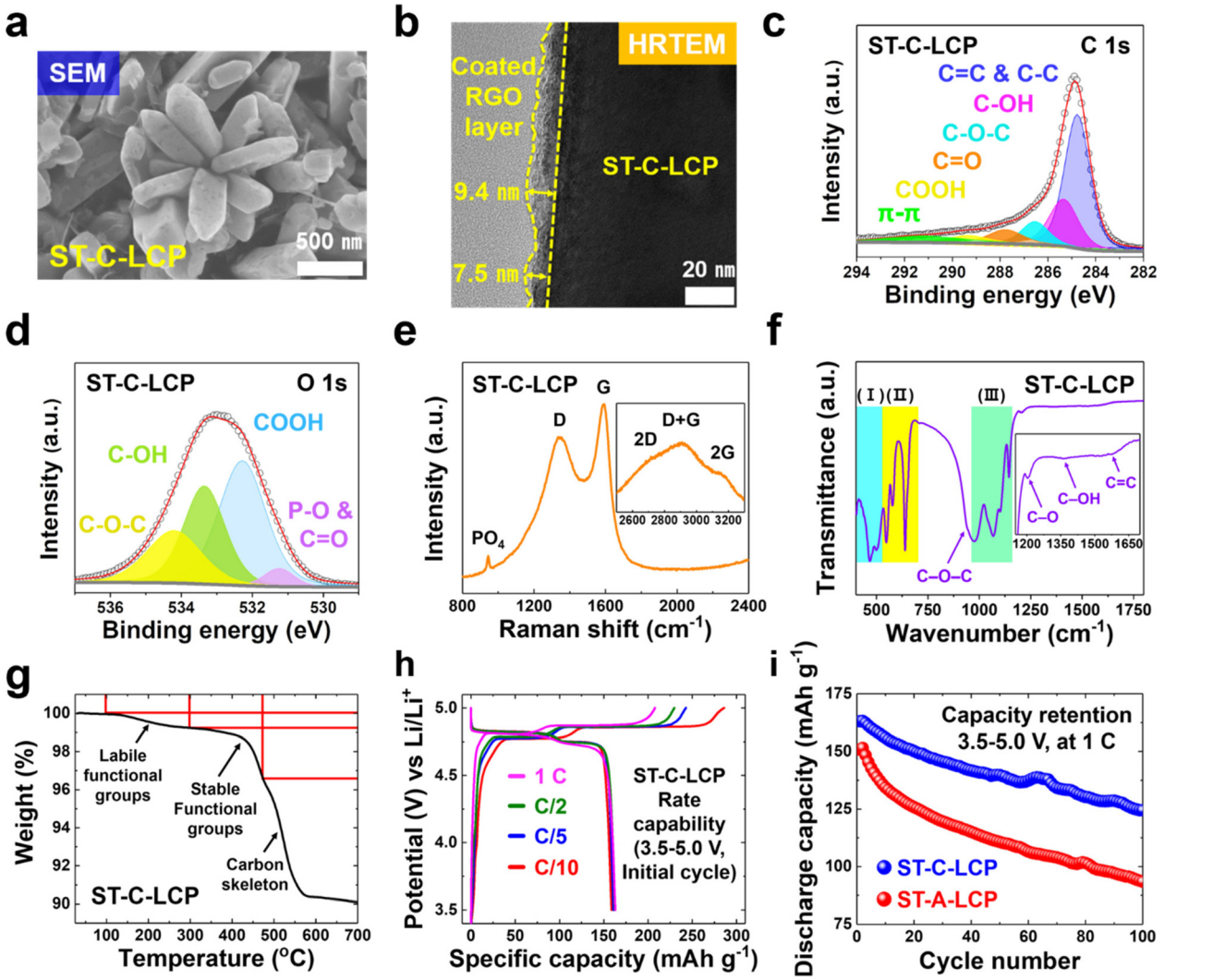

Fig. 2 Structural and electrochemical characterization of the FCL on the ST-C-LCP surface: (a) SEM and (b) HRTEM images; XPS spectra of (c) C 1s and (d) O 1s; (e) Raman, (f) FT-IR, and (g) TGA profile confirming the presence of the FCL and its functional groups; (h) rate capability at various C-rates from C/10 to 1C; and (i) discharge capacity retention of ST-A-LCP and ST-C-LCP within the voltage range 3.5–5.0 V *vs.* Li/Li^+ at 1C.

In order to determine the optimal loading of sucrose, preliminary electrochemical evaluations (Fig. S2) were applied to LCP samples before and after coating. The sample with 40 wt% of sucrose presents the most promising electrochemical results with respect to accessible initial discharge capacity at 1C and retention after 100 cycles compared to the other concentrations. To assess the structural integrity, Rietveld refinement (Fig. S3 and Table S1) confirms that the coated LCP sample retains its phase purity, with only a marginal increase in anti-site defect concentration relative to ST-A-LCP. Moreover, electron microscopy analysis (Fig. 2a and b) reveals that our coating process does not affect the anisotropically grown morphology for the shortened Li-ion diffusion length, while HRTEM imaging displays a continuous and conformal carbonaceous shell of approximately 7–9 nm.[17]

Further spectroscopic techniques (Fig. 2c–f) including XPS, Raman, and FT-IR analyses were carried out to verify the chemical nature of the coated surface layer. In particular, the XPS results show the presence of carbon (C 1s) and oxygen (O 1s). The C 1s spectra (Fig. 2c) were fitted with multiple carbon atom peaks corresponding to non-oxygenated and different oxygen-containing functional groups such as C═C, C–C, C–OH, C–O–C, C═O, COOH, and π–π interactions mediated by delocalized electrons in the aromatic network.[24–27] In addition, the O 1s spectra (Fig. 2d) were deconvoluted into peaks corresponding to the phosphate group (PO_4) and various functional groups such as C═O, COOH, C–OH, and C–O–C.[28,29] The specific binding energies, full width at half maximum (FWHM), and atomic percentage for these identified peaks are listed in Table S2. Collectively, XPS analysis confirms that the coating is predominantly carbonaceous, incorporating a high density of oxygen-containing functional groups. These chemical features imply the successful formation of the functionalized carbon layer (FCL) as a uniform coating layer on the LCP surface.

To validate these findings, Raman and FT-IR spectra were also obtained. The Raman spectrum (Fig. 2e) displays the combined vibration modes at lower and higher Raman shift regions. At the lower shift region, three main vibrations were detected at 944, 1349, and 1593 cm^{-1} corresponding to PO_4, carbon D and G bands, respectively. The second-order bands centered at 2714, 2910, and 3151 cm^{-1} corresponding to 2D, D + G, and 2G peaks are attributed to the overtone and combination of D and G bands. These spectral signatures are indicative of a disordered carbon structure commonly derived from the low-temperature pyrolysis of organic precursors, such as sucrose utilized in this study.[30,31] At the same time, the FT-IR technique was also employed to prove the existence of the FCL on LCP crystals. In principal, both LCP samples before (Fig. S4) and after coating (Fig. 2f) are mainly dominated with three stretching and vibration modes of (I) Li-ion (450–550 cm^{-1}) and (II & III) PO_4^{3-} group (500–700 and 900–1200 cm^{-1}).[32] However, we note that the coated sample exclusively incorporates extra features which are not strong but still persistent, originated from the stretching vibration of functional groups in the FCL such as C–O–C (942 cm^{-1}), C–O (1205 cm^{-1}), C–OH (1363 cm^{-1}), and C=C (1580 cm^{-1}) unlike ST-A-LCP.[33,34] Accordingly, the coating is confirmed as an FCL rich in oxygen-containing functional groups, successfully deposited *via* one-step facile low-temperature pyrolysis of sucrose, and the coated LCP sample is hereafter denoted as ST-C-LCP.

After the confirmation of the FCL, we applied TGA analysis (Fig. 2g) to accurately quantify the FCL derived from sucrose. The entire weight loss was recorded from room temperature to 700 °C with the ramping rate being 10 °C min^{-1} in air. Three distinct sections of weight loss were evidently observed at different temperature ranges: (i) labile oxygen-containing functional group decomposition (100–300 °C, 0.76 wt%), (ii) stabilized oxygen-containing functional group removal (300–450 °C, 2.73 wt%), and (iii) carbon skeleton pyrolysis (450–700 °C, 6.41 wt%).[35,36] On the other hand, the TGA result of ST-A-LCP (Fig. S5) shows the whole mass preserved without any weight loss up to 700 °C. We note that, by simply utilizing 40 wt% sucrose, FCL coating of almost 10 wt% was yielded by the carbonization process during Ar-annealing, as in the case of ST-A-LCP preparation. Moreover, these functional groups facilitate uniform anchoring through strong coordination with LCP surface cations. These polar oxygen species promote rigid coordination interactions, ensuring a homogeneous interfacial coverage across the entire LCP crystals.[37–39] Concurrently, the intrinsic properties of the FCL, specifically its large surface area and superior electronic conductivity, establish an expedited charge-transfer network.[40,41] This interfacial architecture is expected to work synergistically with the bulk-level improvements *via* ST synthesis, which enhances the Li-ion diffusivity.

Reflecting these structural and interfacial modulations, ST-C-LCP demonstrated significantly improved electrochemical performance. Indeed, the exceptional rate capability (Fig. 2h) was observed, with discharge capacities of 158.8, 160.9, 162.6, and 163.0 mAh g^{-1} across all tested C-rates from C/10 to 1C, which nearly approach the theoretical capacity. Thus, the anisotropically grown LCP crystals *via* ST synthesis can be effectively coated with the conductive FCL successfully overcoming the sluggish kinetics by facilitating both Li-ion diffusion and electron transport. Beyond the rate capability, the long-term cycling stability (Fig. 2i) was boosted to 76.36% compared to 61.65% for ST-A-LCP during the initial 100 cycles at 1C. The distinct gap in capacity retention (Fig. S6) is further highlighted by the comprehensive profile throughout the entire cycle periods for both LCP samples. Our proposed coating strategy enhances the cell durability as evident by the number of cycles enabled until the discharge capacity drops to 50 mAh g^{-1} (700 cycles for ST-C-LCP compared to 250 cycles for ST-A-LCP). Notably, ST-C-LCP exhibits improved capacity retention (Fig. S7) over prolonged cycling at relatively faster C-rates (C/5, C/2, and 1C) with the sole exception of C/10.

Furthermore, to provide an objective and broader evaluation, a comparative plot has been introduced in Fig. S8, benchmarking the electrochemical performance of ST-C-LCP against previously reported carbon coating strategies on LCP systems. The plot correlates the cycle number with the final discharge capacity, with distinct symbols assigned to each C-rate to facilitate at-a-glance performance comparison. Notably, the data point corresponding to the present work is positioned toward the upper right region, demonstrating that our FCL delivers outstanding capacity retention compared to the existing literatures. To provide additional context for this comparison, the specific experimental parameters of each surveyed study, including the carbon source, electrode–electrolyte composition, voltage ranges, and initial discharge capacity, are summarized in Table S3.

Nevertheless, the role of the FCL in modulating the electrochemical environment and its subsequent impact on the rate capability and capacity retention are not fully elucidated yet. Therefore, further investigations will be followed to uncover how FCL coating contributes to the enhancements of both charge-transfer kinetics and long-term cycling stability of ST-C-LCP.

Enhanced charge-transfer kinetics *via* the FCL conductive network

To examine the impact of the conductive FCL on charge-transfer kinetics, we initially investigated the statistical distribution of the coulombic efficiency (Fig. 3a and b) recorded over the number of cycles until the discharge capacity reached 50 mAh g^{-1}. This analysis encompasses the entire distribution, mean value, and interquartile range, with the corresponding numerical data presented in Tables S4 and S5. We note that both LCP electrodes exhibit their lowest average coulombic efficiency and widest distribution spread at C/10. This is evidently due to the prolonged exposure of the active material and electrolyte to high-V conditions at the slowest C-rate. Such an extended residence time exacerbates an oxidative degradation at the interface, leading to considerable extra charge capacity.

Meanwhile, as the C-rate increases, the average coulombic efficiency gradually rises, and the statistical distribution significantly narrows. In this regard, the observed trends corroborate the rate-dependent nature of irreversible side reactions,

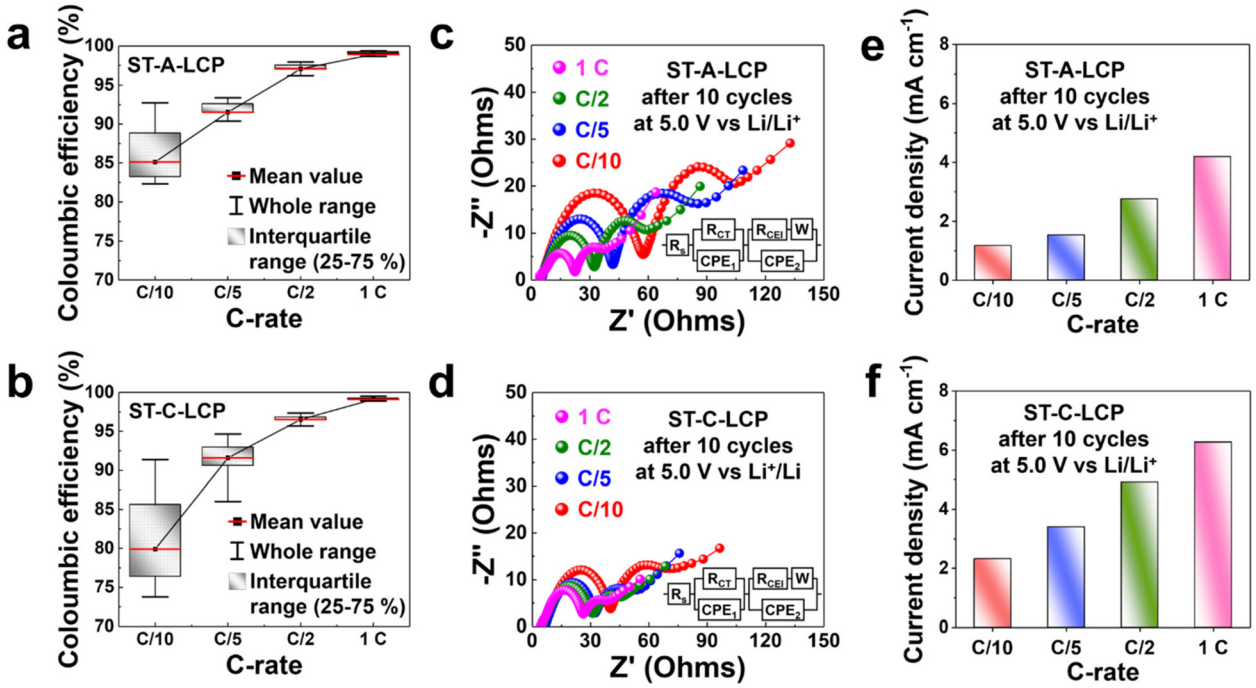

Fig. 3 Comparative post-mortem electrochemical analysis of ST-A-LCP and ST-C-LCP electrodes cycled at various C-rates: (a and b) coulombic efficiency distribution as a function of C-rate; (c and d) EIS analysis (the inset image shows the equivalent circuit model); (e and f) current density measurement from the Nyquist plot under the applied forward bias of 5.0 V *vs.* Li/Li^+.

which can be interpreted as a function of high-V exposure duration. To clearly demonstrate the rate-dependent cycling stability, we compared the average coulombic efficiency under two distinct conditions: C/10 and 1C. At the slowest rate (C/10), ST-C-LCP features the diminished average coulombic efficiency (79.90% *vs.* 85.12% for ST-A-LCP). This finding indicates that electrons generated from oxidative decomposition at high-V are more readily transported to the LCP electrode due to superior electronic conductivity and enlarged active surface area of the FCL resulting in undesired extra charge currents.[40,41] In other words, the FCL serves as a "double-edged sword" as it does improve the rate capability, but cause severe degradation at slower C-rates, which in turn leads to inferior and unevenly distributed coulombic efficiency. However, this drawback is largely mitigated at 1C. Under this condition, ST-C-LCP delivers an enhanced average coulombic efficiency (99.10% *vs.* 98.57% for ST-A-LCP) by effectively curtailing high-V exposure time due to accelerated charge-transfer kinetics. Indeed, as shown in Fig. S9, the coulombic efficiency of both LCP electrodes exhibits comparable values at 1C, indicating that the conductive FCL does not contribute to any significant extra charge capacity at higher rates.

Post-mortem EIS analysis was subsequently performed to substantiate these kinetic advantages. Nyquist plots (Fig. 3c and d) were obtained under the applied forward bias of 5.0 V *vs.* Li/Li^+ for cycled cells, a condition that simulates the delithiation process and captures the resistance encountered as Li-ions migrate from the LCP lattice toward the electrolyte. For all EIS patterns, two semi-circles were observed in high- and mid-frequency regions, in addition to a long tail at low frequency. The formation of the CEI layer during cycling establishes a complex LCP–CEI–electrolyte structure, effectively creating two distinct interfaces. Accordingly, two semi-circles are assigned to the resistance associated with LCP–CEI and CEI–electrolyte interfaces, respectively. In this model, the first semi-circle in the high-frequency region represents the charge-transfer resistance (R_{CT}) at the LCP–CEI interface, where Li-ions are extracted from the LCP lattice. In parallel, the second semi-circle, appearing in the mid-frequency range, corresponds to the resistance (R_{CEI}) at the CEI–electrolyte interface, reflecting the barrier for Li-ions to penetrate the evolved CEI layer and enter the liquid phase. The expansion in the diameters of both semi-circles is attributed to the increased thickness and density of the CEI layer formed under high-V conditions, which hampers efficient Li-ion transport.[42] Notably, both LCP electrodes display enlarged semi-circle diameters at slower C-rates, reflecting a thicker CEI layer due to prolonged high-V exposure that progressively impedes Li-ion intercalation. However, ST-C-LCP demonstrates markedly smaller diameters of high-frequency (R_{CT}) and mid-frequency (R_{CEI}) semi-circles across all C-rates. This significant reduction in resistance confirms that FCL coating effectively mitigates excessive CEI layer growth by expediting charge-transfer kinetics, thereby minimizing the residence time at high-V. These findings are in excellent agreement with the narrower coulombic efficiency distribution observed at 1C, collectively highlighting the role of the FCL in maintaining a stable and thin interfacial architecture.

Moreover, the kinetic implications of the evolving CEI layer are quantitatively evaluated through the current density (Fig. 3e and f) derived from Nyquist plots. These measurements, conducted under the applied forward bias of 5.0 V *vs.* Li/Li^+, further validate the rate-dependent resistance trend discussed above. ST-A-LCP exhibits a significant decline as the C-rate is reduced, yielding values of 4.19, 2.75, 1.53, and 1.17 mA cm^{-1} at 1C, C/2, C/5 and C/10, respectively. In contrast, ST-C-LCP demonstrates a substantial boost in current density across all C-rates, with values increasing by 6.27, 4.91, 3.40, and 2.32 relative to ST-A-LCP at corresponding rates. In addition, ST-C-LCP showed a shortened current density decay period (Fig. S10 and S11) of 200 seconds, compared to 400 seconds observed for ST-A-LCP. These results underscore the intimate correlation between C-rate and progressive CEI evolution. Indeed, slower rates extend the timeframe of high-V exposure, which facilitates thicker CEI formation and subsequently suppresses the current response.

By mitigating this effect, we have demonstrated that the FCL network plays a critical role in accelerating charge-transfer kinetics, thereby providing a fundamental basis for the enhanced rate capability of LCP. This improvement not only paves a way for LCP in niche sectors requiring high power density, but also establishes a fundamental design principle for high-V cathode systems. Specifically, minimizing the high-V exposure duration through the expedited kinetics can serve as an effective strategy for preserving the interfacial integrity, as CEI layer evolution remains inevitable despite incorporating the high-V stabilizing electrolyte additive. Building upon the observed kinetic advantages of FCL coating, the next section further scrutinizes the chemical composition of the CEI layer through XPS analysis to identify the origin of improved long-term cycling stability.

Inorganic-enriched CEI formation *via* the FCL anchoring effect

The correlation between CEI layer composition and prolonged cycle life was probed through post-mortem XPS analysis, as compiled in Fig. 4. All corresponding values, including the binding energy, FWHM, and atomic percentage of each peak, are listed in Tables S6–S9. This investigation compared the pristine electrode as a baseline with cycled electrodes that had reached a discharge capacity at 50 mAh g^{-1} at rates of C/10 and 1C. This comprehensive dataset focuses on three relevant elements of CEI layer composition (C 1s, O 1s, and F 1s) to track the chemical evolution of the interface across two different cycling regimes.

Regarding C1 spectra (Fig. 4a and b) of pristine electrodes, multiple peaks are observed at characteristic binding energies for C–C, C–H, C–O, C═O and O–C═O, originating from the conductive acetylene black.[43] In addition, C–F and CH_2–CF_2 peaks are attributed to PVDF binder, which is another essential electrode component.[44] In the pristine state, ST-C-LCP possesses higher atomic percentages of the carbon skeleton (C–C) and oxygen-containing functional groups (C═O and O–C═O) than those of ST-A-LCP (Tables S6 and S7). This enrichment is directly attributed to the FCL successfully coated on LCP crystals, establishing the integrated conductive carbonaceous network. After cycling at 1C, both electrodes exhibit a relative enhancement in the intensity of most peaks in C 1s spectra, with the exception of the C–C peak (Tables S8 and S9). This trend corroborates progressive CEI layer formation arising from the oxidative decomposition of carbonate solvents (EC, PC, and DMC) and $LiPF_6$ salt in the electrolyte, accelerated by high-V operation.[45,46] Notably, the CH_2–CF_2 peak in the cycled ST-C-LCP increases sharply from 9.79 to 19.07%, whereas ST-A-LCP displays only a marginal rise from 12.54 to 15.90%. This observation implies that the FCL might facilitate the enrichment of fluorinated species at the interface. This compositional shift is further substantiated by F 1s analysis discussed below.

Likewise, O 1s spectra (Fig. 4c and d) reveal distinct compositional changes between the pristine and cycled electrodes for both LCP samples. In the pristine state, ST-C-LCP shows a relatively higher concentration of oxygen-containing functional groups, such as C–O, owing to the integrated FCL coating. We note that upon cycling, the C–O peak intensity becomes remarkably dominant, surging from 3.95 to 42.03% for ST-A-LCP and from 21.26 to 42.08% for ST-C-LCP (Tables S8 and S9). This dramatic chemical shift is intimately related to the oxidative decomposition of carbonate solvents at high-V.

To elucidate the precise driving force behind this high-V degradation, the environmental constraints of cell assembly must be considered. While conventional models for RM dissolution presuppose the presence of trace H_2O and O_2 as prerequisites for acid-driven (*e.g.* hydrogen fluoride, HF) etching, the cell assembly in this study was strictly performed in an anhydrous and anaerobic environment with the moisture and oxygen levels maintained below 0.5 ppm. This stringent control effectively precludes such moisture-dependent pathways as the primary initiation mechanism for early-stage degradation. In these environments, the oxidative decomposition of electrolyte solvents becomes the dominant factor at potentials above 4.5 V. In detail, cyclic carbonates (EC and PC) and their linear counterpart (DMC) undergo ring-opening and C–O bond cleavage, respectively, resulting in polymerization that evolves into β-diketonate-type ligands.[47] The coordination of these ligands with surface RM (Co) cations facilitates interfacial leaching by forming soluble metal–organic complexes. Such coordination involves electron transfer that reduces the oxidation state of Co. This process can be significantly promoted by the chemical instability of the fully delithiated $CoPO_4$ phase.[16,48] Specifically, the trivalent Co is prone to reduction back to the relatively stable divalent state through irreversible side reactions with the electrolyte. The resulting redox tendency might provide an extra thermodynamic driving force to enhance interfacial coordination and subsequent Co dissolution. Consequently, this dissolution process triggers vacancy-induced lattice collapse and structural ingress into the bulk. Thereafter, the soluble metal–organic complexes migrate to and accumulate within the separator and anode, where they undergo electrochemical reduction and deposition during the discharge process. This dissolution and migration mechanism

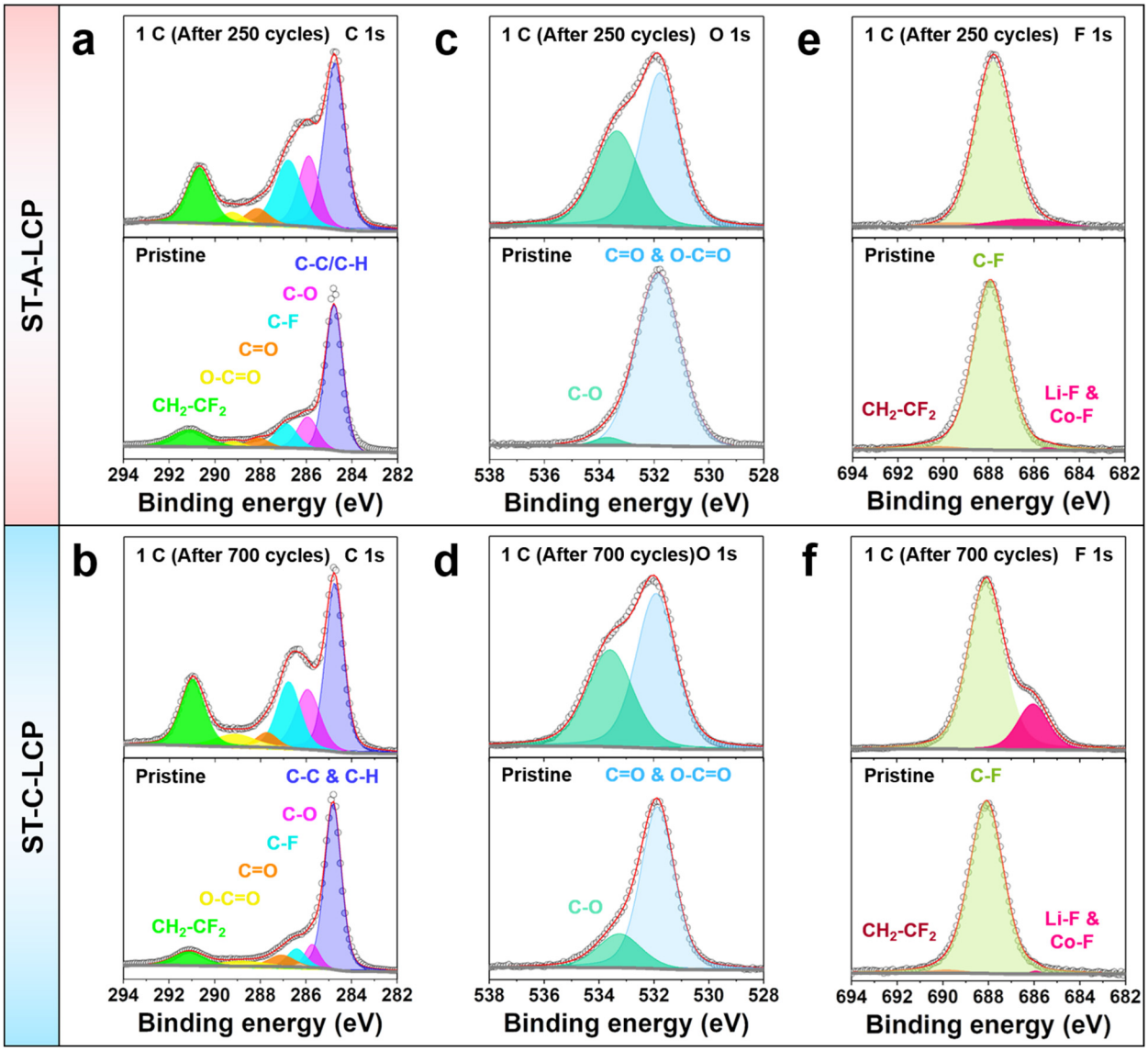

Fig. 4 High-resolution XPS spectra of (a and b) C 1s, (c and d) O 1s, and (e and f) F 1s for the pristine and cycled ST-A-LCP and ST-C-LCP electrodes, illustrating the chemical evolution of the CEI layer after 250 and 700 cycles at 1C, respectively.

fundamentally drives interfacial degradation leading to RM-related capacity loss. Furthermore, this complexation liberates H_2O as a byproduct.[47] The produced moisture further reacts with $LiPF_6$ salt to yield corrosive HF, which exacerbates the collapse of the Co–P–O framework.[49,50] Hence, following this initial coordination-driven dissolution, the synergy between RM dissolution and HF attack establishes a comprehensive interfacial capacity fading mechanism for high-V cathode systems that compromises the overall cell performance.

Unlike the aforementioned elements (C 1s and O 1s), F 1s spectra demonstrate a stark contrast between ST-A-LCP and ST-C-LCP. In the pristine state, both electrodes exhibit nearly identical features, predominantly characterized by a C–F peak originating from PVDF binder. However, distinct CEI layer evolution pathways are observed upon cycling to the same degraded state at a discharge capacity of 50 mAh g^{-1}. Quantitatively, the atomic percentage of inorganic Li–F and Co–F species in the cycled ST-A-LCP electrode marginally increases from 0.65 to 3.82%, whereas ST-C-LCP exhibits a substantial rise from 0.4 to 18.94%. This remarkable inorganic enrichment in ST-C-LCP, *versus* the organic-rich CEI layer in ST-A-LCP, is a direct consequence of the interfacial coordination chemistry engineering enabled by FCL anchoring. The oxygen-containing functional groups in FCL, possessing partially negative charges, effectively stabilize the LCP surface cations and facilitate the formation of an inorganic-enriched CEI layer.[51–53] In turn, this coordination mechanism performs two critical functions: (i) ensuring uniform FCL coverage during fabrication, and (ii) modulating interfacial chemistry throughout electrochemical operation. By anchoring LCP surface cations, this FCL-mediated interface regulation promotes the formation of a stable inorganic-enriched CEI layer.

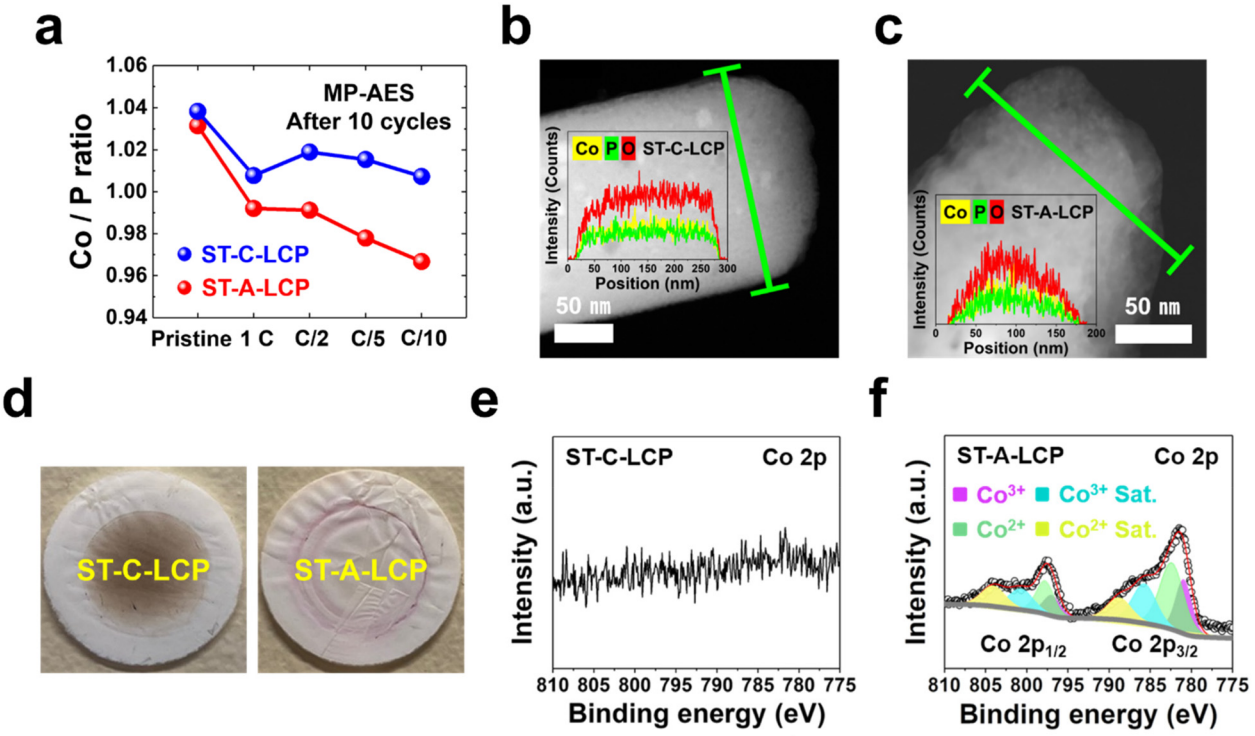

Fig. 5 Evaluation of RM dissolution and parasitic ingress on ST-A-LCP and ST-C-LCP upon cycling: (a) Co/P ratios of the cycled electrodes after 10 cycles at various C-rates, determined *via* MP-AES; (b and c) HAADF images and line scans of the cycled LCP particles after 100 cycles at 1C; (d) photographs and (e and f) corresponding Co 2p XPS spectra of separators retrieved after 100 cycles at 1C.

Building upon our observations, it is postulated that the resulting CEI layer ensures a robust passivation effect, which is likely responsible for the markedly enhanced capacity retention.

Moreover, it should be emphasized that previous research on LCP capacity fading has been largely confined to bulk structural issues and electrochemical side reactions, such as antisite defect and CEI layer evolution.[54–58] However, chemical leaching at the electrode–electrolyte interface remains underexplored despite its significance, as evidenced by the crystal ingress phenomenon observed in this study (Fig. 1c and f). To address this knowledge gap, the following section further demonstrates how effectively this passivation suppresses interfacial degradation.

Interfacial passivation by FCL against RM dissolution and parasitic ingress

To verify the correlation between robust passivation and interfacial stability, Co/P molar ratios (Fig. 5a) were quantified *via* the MP-AES technique for both LCP electrodes after 10 cycles at various C-rates. Pristine electrodes possess near-the stoichiometric Co/P ratio, with marginally 3 and 4% of excess Co for ST-A-LCP and ST-C-LCP, respectively. Relative to these values as a baseline, it is evident that the Co/P ratio of ST-C-LCP remains well-preserved across all C-rates. In contrast, ST-A-LCP exhibits a noticeable reduction as the C-rate decreases. As discussed in the previous sections, a slower C-rate leads to prolonged exposure to high-V conditions, which facilitates Co dissolution through metal–organic complexation. Thus, the observed decline in the Co/P ratio of ST-A-LCP at slower C-rates is attributed to this complexation-driven leaching, whereas the inorganic-enriched CEI layer in ST-C-LCP effectively suppresses this interfacial degradation.

To probe further this phenomenon, we employed TEM techniques including HRTEM, HAADF, and line scanning to examine LCP particles retrieved from electrodes after 100 cycles at 1C. HAADF and HRTEM images (Fig. 5b and S12a) confirm the topographical integrity of ST-C-LCP without parasitic ingress owing to the robust passivation provided by the FCL-mediated interface. Notably, the inset line scan image in Fig. 5b reveals the uniform elemental distributions of Co, P, and O in ST-C-LCP with a rectangular shape. On the other hand, we observed that ST-A-LCP crystal (Fig. 5c and S12b) exhibits pronounced "corrosion" signs and metal depletion, characterized by parasitic ingress that originates at the interface and gradually progressed toward the LCP bulk structure. These results provide clear evidence that FCL coating largely prevents RM dissolution. In addition, these findings underline our postulation that RM dissolution occurring at the interface can be an important contributor to LCP capacity loss rather than the CEI layer alone inducing charge-transfer resistance.

To elucidate the unique passivation chemistry, extra post-mortem studies were undertaken focusing on the separators retrieved from the cycled cells after 100 cycles at 1C. The separators (Fig. 5d) collected from the cycled ST-C-LCP and

ST-A-LCP cells show an obvious optical difference. In particular, the separator from the ST-A-LCP cell is seen to have a pinkish coloration apparently due to migration and deposition on it of dissolved Co species. To further substantiate, we probed the surface of separators *via* XPS characterization. XPS spectra (Fig. 5e and f) clearly present the particular bonding associated with Co detected solely in the separator that was cycled with ST-A-LCP electrodes. Meanwhile, no signal for RM dissolution is identified in ST-C-LCP even after undergoing the same number of charge–discharge cycles. Furthermore, the separator from ST-A-LCP cells reveals two different oxidation states of Co (Co^{2+} and Co^{3+}) simultaneously. Following the deconvolution of the Co 2p spectrum (Co $2p_{3/2}$ and Co $2p_{1/2}$), the relative atomic ratio of Co^{2+} and Co^{3+} (Table S10) was determined to be approximately 64.6 and 35.4%, respectively. We note that this value closely corresponds to the intermediate phase $Li_{2/3}Co^{2+}{}_{2/3}Co^{3+}{}_{1/3}PO_4$ formed during the Li-ion intercalation process.[59–61] This is consistent with the shrinking core model of LCP, where the intermediate phase persists at the electrode–electrolyte interface for the longest duration upon (de)intercalation.[59] Consequently, this intermediate phase serves as the primary source of the dissolved species with mixed oxidation states of Co detected in the separator. These findings clearly prove that parasitic ingress on the particle surface is the result of RM dissolution when LCP is exposed to high-V upon electrochemical cycling regardless of charge and discharge steps, since the redox reactions of RM ($Co^{2+} \leftrightarrow Co^{3+}$) initiate at the interface at high-V.[62–64] In contrast, FCL anchoring facilitates the formation of an inorganic-enriched CEI layer, which acts as a robust physical and chemical barrier. This passivation layer mitigates the complexation-driven leaching of RM cations, thereby maintaining the structural and compositional integrity of the LCP surface.

Conclusion

In this work, we performed systematic post-mortem analysis of LCP cathodes to elucidate the interphasial degradation mechanism and advance an interfacial coordination chemistry engineering strategy *via* FCL anchoring to mitigate the resulting detrimental effects. Our findings revealed that high-V operation triggers RM dissolution from the olivine lattice, serving as another critical contributor to capacity fading distinct from conventional anti-site defect and CEI evolution. Notably, this degradation is governed by the total high-V exposure duration upon cycling, which necessitates enhanced rate capability to mitigate such interfacial damage. These insights motivated us to develop the sucrose-derived FCL anchoring strategy. This approach aims to facilitate expedited charge exchange and regulate interfacial coordination chemistry, thereby markedly suppressing the undesirable side reactions at the interface. Specifically, oxygen-containing functional groups anchor surface cations, promoting the formation of a protective inorganic-enriched CEI layer predominantly composed of Li–F and Co–F that effectively inhibits RM dissolution. Consequently, this multi-functional interface enables outstanding rate capability (163.0 mAh g^{-1} at 1C) with significantly enhanced retention (76.36% after 100 cycles). The integration of preferential crystal engineering and FCL-mediated interfacial stabilization establishes practical design principles for high-V polyanionic cathodes. Furthermore, these optimized, defect-free LCP crystals can be subsequently enhanced through tailored doping scenarios and integration with solid-state electrolytes to achieve superior cycling stability even at 5.0 V (*vs.* Li/Li^+) operation. Ultimately, this work establishes a practical high-V cathode model and paves the way for high energy density LCP systems with an extended cycle life.

Experimental section

Materials preparation

LCP materials were synthesized *via* a solvothermal (ST) process utilizing ethylene glycol (EG) as a reaction medium at 260 °C for 6-hour duration with agitation at 300 rpm. The precursor solution was prepared with a specific molar ratio of $Li : Co : PO_4 = 2 : 1 : 1$, while the concentrations of Co and PO_4 sources were maintained at 0.4 M. The comprehensive details regarding the chemicals and synthetic procedures are documented in our previous reports.[17,32] This methodology is specifically designed to facilitate the preferential anisotropic crystal growth. For sucrose-derived functionalized carbon layer (FCL) coating, the method involved dispersion and stirring of pristine ST-LCP in deoxygenated deionized water containing sucrose (99.5%, $C_{12}H_{22}O_{11}$, Sigma-Aldrich) of different weight percents (0, 30, 40, 50 wt%). The well-mixed suspension was transferred to an alumina crucible. The slurry was then dried in a vacuum oven at 80 °C and transferred to an MTI mini tube furnace (model OTF-1200X) and heated at 700 °C for 1 hour with a continuous Ar gas flow to induce sucrose decomposition and subsequent carbonization. The samples after Ar-annealing are denoted as 'ST-A-LCP' (without sucrose) and 'ST-C-LCP' (with sucrose).

Materials characterization

High-resolution transmission electron microscopy (HRTEM) with high-angle annular dark-field (HAADF) imaging and energy dispersive X-ray (EDS) analysis for elemental mapping was applied to monitor the evolved CEI and FCL using a Thermo Scientific Talos F200X G2 STEM with the accelerating voltage of 200 kV. The morphology of LCP samples was evaluated with a Hitachi cold-field emission SU-8000 scanning electron microscope (CFE-SEM). Thermogravimetic analysis (TGA) was performed in air from room temperature to 700 °C with the heating rate at 10 °C min^{-1} using a TGA 5500 thermal analyzer and platinum crucibles for quantitative analysis of the CEI and FCL. For the surface layer composition analysis, X-ray photoelectron spectroscopy (XPS) measurements were made with Thermo Scientific K-Alpha using an aluminum (Al) Kα micro-focused monochromator. XPS data processing was performed with Avantage data system for peak fitting. Powder

X-ray diffraction (PXRD) patterns were collected with a Bruker D8 Discovery X-ray diffractometer using Co Kα radiation with the wavelength (λ) of 1.78892 Å from 2θ = 10 to 80°. Crystal structure information for lattice parameters and anti-site defect concentration was fitted and estimated with XRD Rietveld refinement by using TOPAS Academic V5 software. The microwave plasma atomic emission spectrometer (MP-AES) from Agilent was used to determine the concentration ratio of the remaining cobalt to phosphate (Co/P) in LCP retrieved from the cycled electrodes. Prior to MP-AES measurements, the cycled electrodes were soaked in ethanol and sonicated for 3 hours to separate the LCP active material from acetylene black and PVDF binder. Subsequently, they were digested by using 50 vol% concentrated hydrochloric acid (HCl, Fisher Scientific) followed by dilution with 4 vol% nitric acid (TraceMetal Grade, HNO_3, Fisher Scientific). Raman spectroscopy (DXR2 Raman Microscope, Thermo Scientific) with 532 nm wavelength and Fourier transform infrared (FT-IR) spectroscopy (PerkinElmer Spectrum II FT-IR Spectrometer) were employed in the wavenumber range of 4000 to 400 cm^{-1} with a resolution of 0.5 cm^{-1} to confirm the existence of the FCL and its oxygen-containing functional groups on the surface of the ST-C-LCP sample.

Battery assembly and electrochemical protocols

To fabricate the cathode electrode slurry, the active material (ST-A-LCP and ST-C-LCP), conductive acetylene black (Alfa Aesar), and polyvinylidene fluoride (PVDF, $(C_2H_2F_2)_n$, Sigma-Aldrich) binder were mixed in *N*-methyl-2-pyrrolidone (NMP, 99.5% C_5H_9NO, Sigma-Aldrich) solvent with a weight ratio of 7 : 2 : 1, corresponding to 140 mg, 40 mg, and 20 mg, respectively. The slurry was pasted on a high-purity Al foil current collector and then dried overnight at 80 °C in a vacuum oven. The cathode electrodes were prepared with a diameter of 1 cm and a thickness of 0.3 mm, achieving an average mass loading of 2–2.5 mg cm^{-2}. Lithium (Li) metal (MSE Supplies) and polypropylene film (Celgard 2200) were used as anodes and separators. The customized electrolyte solution was prepared by dissolving 1 M lithium hexafluorophosphate (>97% $LiPF_6$, TCI Chemicals) solution in a 1 : 1 : 3 (vol%) mixture of ethylene carbonate (EC, 99% $(CH_2O)_2CO$, Sigma-Aldrich), propylene carbonate (PC, 99.7% $CH_3C_2H_3O_2CO$, Sigma-Aldrich), and dimethyl carbonate (DMC, 99% $H_3COCOOCH_3$, Sigma-Aldrich) carbonate solvents, incorporating 2 wt% tris(trimethylsilyl) phosphite (95% $[(CH_3)_3SiO]_3P$, Sigma-Aldrich) as a high-V stabilizing additive. The galvanostatic charge–discharge profile was measured on an Arbin cycler at an ambient temperature of 25 °C. The battery cycling test was carried out at different C-rates (1C = 167 mAh g^{-1}) in the voltage range of 3.5–5.0 V *vs.* Li/Li^+. For capacity retention, we continued the cycling tests until the discharge capacity declined to 50 mAh g^{-1}. Electrochemical impedance spectroscopy (EIS) measurements of the pristine and cycled electrodes were made using a BioLogic workstation in potentiostatic mode between 1 MHz and 10 mHz with the forward bias potentials (5.0 V *vs.* Li/Li^+). Nyquist plots were fitted using ZView® software. The electrochemical data presented in this work correspond to the representative cell performance that closely matches the median values of capacity and retention.

Post-mortem analysis

After performing the above-described electrochemical tests, the cycled electrodes and separators were harvested in an Ar-filled glovebox (H_2O and O_2 < 0.5 ppm) and rinsed with DMC three times to remove the residual electrolyte and Li salt. Subsequently, the collected electrodes and separators were dried in the glovebox for 48 hours. Further characterization for the crystal structure, surface, and elemental composition was carried out with the same protocols outlined above.

Author contributions

M. Woo performed all the experiments and characterization with the interpretation of the results. G. P. Demopoulos supervised all aspects of the research.

Conflicts of interest

There are no conflicts to declare.

Data availability

The data that support the findings of this study have been included as part of the supplementary information (SI). Further information is available from the corresponding author upon reasonable request.

Supplementary information is available. See DOI: https://doi.org/10.1039/d6eb00077k.

Acknowledgements

This research project funded by the Natural Sciences & Engineering Research Council of Canada [NSERC Strategic Project Grant Number: NSERC STPGP 521217-18] was sponsored by Hydro-Québec's Centre of Excellence on Transportation Electrification and Energy Storage. Additional support *via* the McGill Engineering Doctoral Award program is gratefully acknowledged.

References

1 Z. Zhu, T. Jiang, M. Ali, Y. Meng, Y. Jin, Y. Cui and W. Chen, *Chem. Rev.*, 2022, **122**, 16610–16751.
2 V. Viswanathan, A. H. Epstein, Y.-M. Chiang, E. Takeuchi, M. Bradley, J. Langford and M. Winter, *Nature*, 2022, **601**, 519–525.
3 M. Dixit, A. Bisht, R. Essehli, R. Amin, C.-B. M. Kweon and I. Belharouak, *ACS Energy Lett.*, 2024, **9**, 934–940.

4 D. McNulty, A. Hennessy, M. Li, E. Armstrong and K. M. Ryan, *J. Power Sources*, 2022, **545**, 231943.
5 C. Liu, Z. G. Neale and G. Cao, *Mater. Today*, 2016, **19**, 109–123.
6 A. Konarov, S.-T. Myung and Y.-K. Sun, *ACS Energy Lett.*, 2017, **2**, 703–708.
7 A. M. Nolan, Y. Liu and Y. Mo, *ACS Energy Lett.*, 2019, **4**, 2444–2451.
8 W. Li, B. Song and A. Manthiram, *Chem. Soc. Rev.*, 2017, **46**, 3006–3059.
9 A. K. Padhi, K. S. Nanjundaswamy and J. B. Goodenough, *J. Electrochem. Soc.*, 1997, **144**, 1188.
10 C. Masquelier and L. Croguennec, *Chem. Rev.*, 2013, **113**, 6552–6591.
11 Y.-M. Kang, Y.-I. Kim, M.-W. Oh, R.-Z. Yin, Y. Lee, D.-W. Han, H.-S. Kwon, J. H. Kim and G. Ramanath, *Energy Environ. Sci.*, 2011, **4**, 4978–4983.
12 D. Liu, W. Zhu, C. Kim, M. Cho, A. Guerfi, S. A. Delp, J. L. Allen, T. R. Jow and K. Zaghib, *J. Power Sources*, 2018, **388**, 52–56.
13 J. Wu and C.-J. Tsai, *ACS Appl. Energy Mater.*, 2021, **4**, 6408–6413.
14 Y. Maeyoshi, S. Miyamoto, Y. Noda, H. Munakata and K. Kanamura, *J. Power Sources*, 2017, **337**, 92–99.
15 X. Wu, M. Meledina, J. Barthel, Z. Liu, H. Tempel, H. Kungl, J. Mayer and R.-A. Eichel, *Energy Storage Mater.*, 2019, **22**, 138–146.
16 J. G. Lapping, S. A. Delp, J. L. Allen, J. L. Allen, J. W. Freeland, M. D. Johannes, L. Hu, D. T. Tran, T. R. Jow and J. Cabana, *Chem. Mater.*, 2018, **30**, 1898–1906.
17 M. Woo, S.-W. Park, J. Lee, D.-H. Seo and G. P. Demopoulos, *Adv. Energy Mater.*, 2025, **15**, 2404404.
18 M. Woo, J. Lee and G. P. Demopoulos, *Mater. Adv.*, 2023, **4**, 4823–4834.
19 A. Tornheim, S. Sharifi-Asl, J. C. Garcia, J. Bareño, H. Iddir, R. Shahbazian-Yassar and Z. Zhang, *Nano Energy*, 2019, **55**, 216–225.
20 N. R. Park, Y. Li, W. Yao, M. Zhang, B. Han, C. Mejia, B. Sayahpour, R. Shimizu, B. Bhamwala, B. Dang, S. Kumakura, W. Li and Y. S. Meng, *Adv. Funct. Mater.*, 2023, **34**, 2312091.
21 M. Uitz, M. Sternad, S. Breuer, C. Täubert, T. Traußnig, V. Hennige, I. Hanzu and M. Wilkening, *J. Electrochem. Soc.*, 2017, **164**, A3503.
22 W. M. Dose, W. Li, I. Temprano, C. A. O'Keefe, B. L. Mehdi, M. F. L. D. Volder and C. P. Grey, *ACS Energy Lett.*, 2022, **7**, 3524–3530.
23 T. He, R. Jia, X. Lang, X. Wu and Y. Wang, *J. Electrochem. Soc.*, 2017, **164**, E379.
24 W. Tang, *J. Mater. Chem.*, 2004, **14**, 3457–3461.
25 R. Wang, Y. Wang, C. Xu, J. Sun and L. Gao, *RSC Adv.*, 2013, **3**, 1194–1200.
26 A. Kovtun, D. Jones, S. Dell'Elce, E. Treossi, A. Liscio and V. Palermo, *Carbon*, 2019, **143**, 268–275.
27 F. J. Sonia, H. Kalita, M. Aslam and A. Mukhopadhyay, *Nanoscale*, 2017, **9**, 11303–11317.
28 B. D. Ossonona and D. Bélanger, *RSC Adv.*, 2017, **7**, 27224–27234.
29 Y. C. G. Kwan, G. M. Ng and C. H. A. Huan, *Thin Solid Films*, 2015, **590**, 40–48.
30 M. A. Pimenta, G. Dresselhaus, M. S. Dresselhaus, L. G. Cançado, A. Jorioa and R. Saito, *Phys. Chem. Chem. Phys.*, 2007, **9**, 1276–1290.
31 R. Yuan, Y. Guo, I. Gurgan, N. Siddique, Y.-S. Li, S. Jang, G. A. Noh and S. H. Kim, *Carbon*, 2025, **238**, 120214.
32 K. K. H. D. Silva, P. Viswanath, V. K. Rao, S. Suzuki and M. Yoshimura, *J. Phys. Chem. C*, 2021, **125**, 7791–7798.
33 C. R. Minitha, V. S. Anithaa, V. Subramaniam and R. T. R. Kumar, *ACS Omega*, 2018, **3**, 4105–4112.
34 E. Mahmud and M. R. Islam, *Sci. Rep.*, 2023, **13**, 20967.
35 J. Shen, Y. Hu, M. Shi, X. Lu, C. Qin, C. Li and M. Ye, *Chem. Mater.*, 2009, **21**, 3514–3520.
36 D. C. Marcano, D. V. Kosynkin, J. M. Berlin, A. Sinitskii, Z. Sun, A. Slesarev, L. B. Alemany, W. Lu and J. M. Tour, *ACS Nano*, 2010, **4**, 4806–4814.
37 W. Liu and G. Speranza, *ACS Omega*, 2021, **6**, 6195–6205.
38 Y. Li, J. Liu, X. Wang, X. Zhang, N. Chen, L. Qian, Y. Zhang, X. Wang and Z. Chen, *Small Sci.*, 2023, **3**, 2300045.
39 D. Xiong, X. Li, H. Shan, Y. Zhao, L. Dong, H. Xu, X. Zhang, D. Li and X. Sun, *Electrochim. Acta*, 2015, **174**, 762–769.
40 D. Y. Ko, H. J. Kim, H. Park, E. Kim and H. Kim, *ACS Nano*, 2025, **19**, 16957–16966.
41 Y. Shi, L. Wen, H. Yang, Z. Sun and F. Li, *J. Mater. Chem. A*, 2025, **13**, 36802–36824.
42 N. Zhang, B. Wang, F. Jin, Y. Chen, Y. Jiang, C. Bao, J. Tian, J. Wang, R. Xu, Y. Li, Q. Lv, H. Ren, D. Wang, H. Liu, S. Dou and X. Hong, *Cell Rep. Phys. Sci.*, 2022, **3**, 101197.
43 R. Tatara, P. Karayaylali, Y. Yu, Y. Zhang, L. Giordano, F. Maglia, R. Jung, J. P. Schmidt, I. Lund and Y. Shao-Horn, *J. Electrochem. Soc.*, 2019, **166**, A5090.
44 J.-B. Gieu, V. Winkler, C. Courrèges, L. E. Ouatani, C. Tessier and H. Martinez, *J. Mater. Chem. A*, 2017, **5**, 15315–15325.
45 Z. Arthur, H.-C. Chiu, X. Lu, N. Chen, V. Emond, K. Zaghib, D.-T. Jiang and G. P. Demopoulos, *Chem. Commun.*, 2016, **52**, 190–193.
46 Q. Li, Y. Wang, X. Wang, X. Sun, J.-N. Zhang, X. Yu and H. Li, *ACS Appl. Mater. Interfaces*, 2019, **12**, 2319–2326.
47 A. Jarry, S. Gottis, Y.-S. Yu, J. Roque-Rosell, C. Kim, J. Cabana, J. Kerr and R. Kostecki, *J. Am. Chem. Soc.*, 2015, **137**, 3533–3539.
48 L. Wheatcroft, T. D. Tran, D. Özkaya, J. Cookson and B. J. Inkson, *ACS Appl. Energy Mater.*, 2022, **5**, 196–206.
49 J. L. Tebbe, A. M. Holder and C. B. Musgrave, *ACS Appl. Mater. Interfaces*, 2015, **7**, 24265–24278.
50 Y. Ma, Y. Zhou, C. Du, P. Zuo, X. Cheng, L. Han, D. Nordlund, Y. Gao, G. Yin, H. L. Xin, M. M. Doeff, F. Lin and G. Chen, *Chem. Mater.*, 2017, **29**, 2141–2149.
51 S. Wolf, M. Roschger, B. Genorio, D. Garstenauer and V. Hacker, *ACS Omega*, 2023, **8**, 11536–11543.
52 P. V. Kamat, *J. Phys. Chem. Lett.*, 2009, **1**, 520–527.
53 L. Liu, X. Zhao, G. Ding, C. Han and J. Liu, *Chem. Eng. J.*, 2023, **470**, 143820.

54 J. L. Allen, T. R. Jow and J. Wolfenstine, *J. Power Sources*, 2011, **196**, 8656–8661.
55 E. Markevich, R. Sharabi, H. Gottlieb, V. Borgel, K. Fridman, G. Salitra, D. Aurbach, G. Semrau, M. A. Schmidt, N. Schall and C. Bruenig, *Electrochem. Commun.*, 2012, **15**, 22–25.
56 Q. D. Truong, M. K. Devaraju, T. Tomai and I. Honma, *ACS Appl. Mater. Interfaces*, 2013, **5**, 9926–9932.
57 E. Markevich, G. Salitra, K. Fridman, R. Sharabi, G. Gershinsky, A. Garsuch, G. Semrau, M. A. Schmidt and D. Aurbach, *Langmuir*, 2014, **30**, 7414–7424.
58 Y. H. Ikuhara, X. Gao, C. A. J. Fisher, A. Kuwabara, H. Moriwake, K. Kohama, H. Iba and Y. Ikuhara, *J. Mater. Chem. A*, 2017, **5**, 9329–9338.
59 M. G. Palmer, J. T. Frith, A. L. Hector, A. W. Lodge, J. R. Owen, C. Nicklinb and J. Rawle, *Chem. Commun.*, 2016, **52**, 14169–14172.
60 J. L. Allen, J. L. Allen, T. Thompson, S. A. Delp, J. Wolfenstine and T. R. Jow, *J. Power Sources*, 2016, **327**, 229–234.
61 F. C. Strobridge, R. J. Clément, M. Leskes, D. S. Middlemiss, O. J. Borkiewicz, K. M. Wiaderek, K. W. Chapman, P. J. Chupas and C. P. Grey, *Chem. Mater.*, 2014, **26**, 6193–6205.
62 S. Sreedeep, S. Natarajan and V. Aravindan, *Curr. Opin. Electrochem.*, 2022, **31**, 100868.
63 W. M. Dose, I. Temprano, J. P. Allen, E. Björklund, C. A. O'Keefe, W. Li, B. L. Mehdi, R. S. Weatherup, M. F. L. D. Volder and C. P. Grey, *ACS Appl. Mater. Interfaces*, 2022, **14**, 13206–13222.
64 M. Gauthier, T. J. Carney, A. Grimaud, L. Giordano, N. Pour, H.-H. Chang, D. P. Fenning, S. F. Lux, O. Paschos, C. Bauer, F. Maglia, S. Lupart, P. Lamp and Y. Shao-Horn, *J. Phys. Chem. Lett.*, 2015, **6**, 4653–4672.